



Strain-dependent one-dimensional confinement channels in twisted bilayer 1T'-WTe₂

S. J. Magorrian  and N. D. M. Hine *Department of Physics, *University of Warwick*, Coventry CV4 7AL, United Kingdom

(Received 30 April 2024; accepted 24 June 2024; published 8 July 2024)

The low-symmetry and anisotropic lattice of 1T' WTe₂ is responsible for the existence of parallel one-dimensional channels in the moiré patterns of twisted bilayers. This gives the opportunity to explore moiré physics of a different nature to that widely observed in twisted bilayers of materials with hexagonal symmetries. Here, we combine plane-wave and linear-scaling density functional theory calculations to describe the electronic properties of twisted bilayer 1T' WTe₂. We investigate the strain dependence of both aligned bilayer configurations across a range of stacking geometries, and of the twisted bilayer itself. For a small change in the lattice parameters of the constituent 1T' WTe₂ monolayers, we find a very substantial increase in the moiré-induced striped electrostatic potential landscape in the twisted bilayer. We measure a peak-to-trough magnitude > 200 meV between parallel linear channels, sufficient to induce Luttinger liquid behavior.

DOI: [10.1103/PhysRevB.110.045410](https://doi.org/10.1103/PhysRevB.110.045410)

I. INTRODUCTION

The novel and interesting physics arising from the long-range periodicity present in the moiré patterns of twisted bilayers of two-dimensional (2D) materials with hexagonal symmetry, such as graphene [1–4] and the transition-metal dichalcogenides (TMDCs) [5–9], has given rise to extensive research into the physical phenomena hosted in these systems. Typical twisted bilayers of TMDCs comprised of monolayers exfoliated from 2H-polytype crystals feature moiré superlattices with hexagonal patterns and symmetries inherited from the symmetries of their constituent monolayers [10].

More recently, attention has turned to different, usually lower, symmetries in moiré superlattices of 2D materials. Such a lowering of symmetry can be achieved by application of strain to previously hexagonal twisted bilayer systems [11,12], or by construction of twisted bilayers from nonhexagonal 2D material monolayers. Systems in the latter case include GeSe [13], phosphorene [14], and the 1T' phase of the TMDCs. Among the TMDCs (MX_2 , $M = \text{Mo, W}$; $X = \text{S, Se, Te}$) the hexagonal 2H polytype is generally energetically favored over 1T' [15], with only WTe₂ having the 1T' phase as the most stable. This phase of WTe₂ [16], the structure of which is shown in the top panels of Fig. 1, features distorted atomic layers, and a rectangular primitive cell.

Owing to the reduced symmetry and anisotropy of the distorted monolayer, twisted bilayer 1T' WTe₂ has a qualitatively different moiré pattern to that familiar in twisted bilayers of the 2H phase. Whereas moiré patterns constructed from

hexagonal structures cannot easily break the threefold symmetry that prevents the emergence of any linear features over long distances, in 1T' such features emerge naturally from the rectangular symmetry. This is demonstrated in the moiré supercell of twisted bilayer 1T' WTe₂ with twist angle $\theta = 4.66^\circ$, illustrated in Fig. 2. The moiré supercell is rectangular, inherited from the rectangular primitive cell of monolayer 1T' WTe₂, while the chains of the tungsten sublattices form one-dimensional stripes in the moiré pattern. Transport experiments on twisted bilayer 1T' WTe₂ with a twist angle $\sim 5^\circ$ [17] revealed highly anisotropic transport properties, with conductance across the stripes in the moiré pattern exhibiting a power-law scaling consistent with the formation of a 2D array of 1D electronic channels hosting Luttinger liquid (LL) behavior. Subsequent investigations confirmed this LL behavior and investigated its robustness down to millikelvin temperatures [18]. In Luttinger liquid materials, a crossover temperature T^* is thought to exist below which the LL state gives way to a 2D Fermi liquid, previously estimated as $T^* \sim t_\perp (t_\perp/t_\parallel)^{\eta/(1-\eta)}$, where t_\perp is interwire hopping and t_\parallel intrawire hopping, and η is the power-law exponent associated with the DOS at the 1D Fermi surface [19]. The existence of LL behavior down to millikelvin temperatures is thus indicative of strong confinement to 1D channels.

The monolayer band structure of 1T' WTe₂, which we illustrate via density functional theory (DFT) calculations shown in Fig. 1 and described in Sec. II, features a hole pocket at Γ , flanked by two electron pockets. In the absence of spin-orbit coupling (SOC), there is a protected band crossing near the minimum of the electron pocket. SOC lifts this degeneracy, depending on the overlap between the electron and hole pockets this results in either a semimetallic or gapped band structure. Due to an inversion between the two bands involved 1T' WTe₂ has long been predicted theoretically to host in the monolayer gapped quantum spin Hall (QSH) insulating behavior [20,21]. Following the theoretical predictions of QSH behavior in 1T' WTe₂, experimental confirmation of inverted

*Contact author: n.d.m.hine@warwick.ac.uk

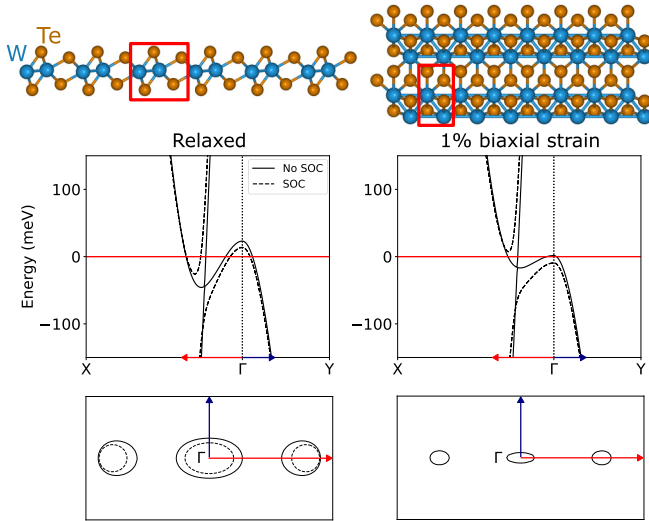


FIG. 1. Top panels: Side and top views of monolayer $1T'$ - WTe_2 , with red boxes highlighting the primitive unit cell of the system. Middle panels: Band structures of relaxed and 1% biaxially strained monolayer $1T'$ WTe_2 , based on DFT calculations. Solid and dashed lines are for calculations neglecting and including spin-orbit coupling (SOC), respectively. Bottom panels: Fermi contours extracted from the band structures shown. Blue and red arrows indicate extent of regions mapped to show Fermi contours.

bands has been obtained, with a spin-orbit-induced gap and a conducting edge state [22–27] observed, while strain tunability between a semimetallic phase and a gapped phase has been reported [28]. Evidence has also been found [29,30] indicating that the gap-opening mechanism in monolayer $1T'$ WTe_2 is the formation of electron-hole pairs, forming an excitonic insulator at charge neutrality, as opposed to the system being a simple band insulator or electron localization being responsible for the formation of a gap.

Few-layer films and bulk crystals of $1T'$ WTe_2 have been observed to exhibit ferroelectric polarization despite being metallic [31,32], with switching achieved via a small relative in-plane shift between the layers [33,34]. In the bulk the topologically rich nature of $1T'$ WTe_2 appears in its character as a type-II Weyl semimetal [35]. In twisted bilayers, angle-resolved photoemission spectroscopy has confirmed the presence of electron pockets and twist-angle dependence of band structure around the Fermi level [36].

In this work, we carry out first-principles modeling of twisted bilayers of $1T'$ to investigate the properties of the low-symmetry striped moiré patterns of twisted bilayer $1T'$ WTe_2 . These simulations combine plane-wave density functional theory (DFT) calculations for primitive-cell aligned bilayers of WTe_2 with a direct linear-scaling DFT calculation for a large low-strain supercell of twisted bilayer WTe_2 , with a twist angle of 4.66° . We illustrate the moiré supercell in Fig. 2. This supercell features alternating one-dimensional stripes in which the chains of tungsten atoms in the two layers are either maximally misaligned or vertically opposite each other, regions labeled A and C, respectively, in Fig. 2.

Examination of the difference between the electrostatic potential of the twisted bilayer and the sum of the

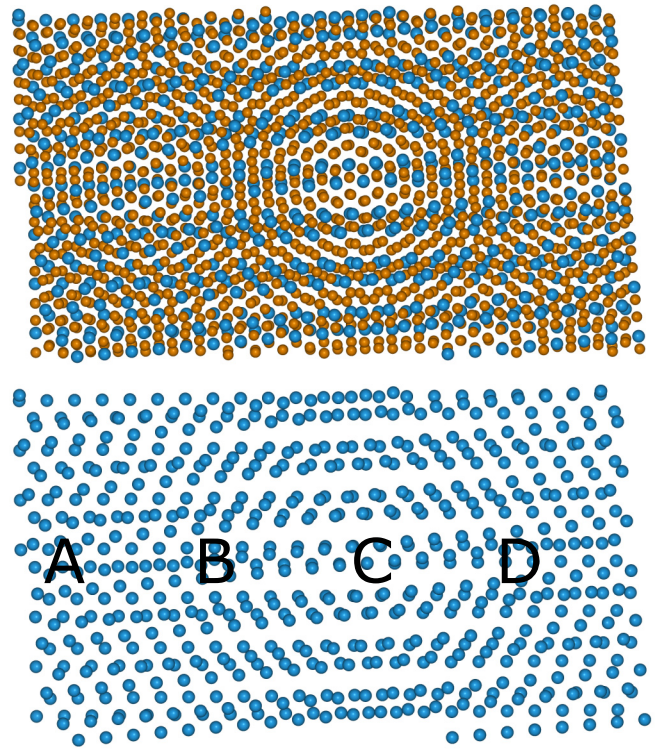


FIG. 2. Top panel: Supercell twisted bilayer $1T'$ - WTe_2 with twist angle $\theta = 4.66^\circ$ used in LS-DFT calculations. Bottom panel: Structure of twisted bilayer showing only tungsten atoms, highlighting one-dimensional channel in the moiré pattern. A–D mark regions with local atomic registries for which aligned bilayer band structures are presented in Fig. 5. At C the chains of tungsten atoms are vertically opposite each other in the two layers, at A they are maximally misaligned. B and D are intermediate configurations.

potentials of isolated monolayers reveals the twisted bilayer has an instability under a small adjustment in the lattice of the constituent monolayers. On application of 1% biaxial strain a confining potential wave on the scale of the one-dimensional striped moiré pattern forms, with a peak-to-trough magnitude > 200 meV. This is larger by 1–2 orders of magnitude than the hopping energies associated with confinement previously observed to provide sufficient suppression of interchannel hopping to observe LL behavior in organic quasi-1D conductors [19]. We calculate spectral functions for the twisted bilayer unfolded and projected onto the primitive cells of the constituent monolayers, revealing a substantial disruption to the band structure due to the confining potential wave in the strained case. Finally, we calculate using plane-wave DFT band structures for aligned primitive bilayers of $1T'$ WTe_2 with stackings corresponding to the local atomic registries found in different regions of the moiré supercell of the twisted bilayer. These show notable changes in topology both on changing the local bilayer stacking order, and on application of a small strain.

II. METHODS

To obtain a relaxed monolayer geometry for $1T'$ WTe_2 we carried out plane-wave DFT calculations using the QUANTUM

ESPRESSO package [37,38]. The generalized gradient approximation of Perdew, Burke, and Ernzerhof is used [39] with projector-augmented wave (PAW) pseudopotentials generated via a fully relativistic calculation [40] with spin-orbit coupling taken into account. For the plane-wave DFT calculations neglecting spin-orbit coupling (SOC) we use pseudopotentials from the JTH data set [41], which are generated using a scalar-relativistic approximation. Cutoffs of 80 Ry and 720 Ry are used for the wave functions and the density, respectively.

Direct atomistic simulation of twisted bilayers of two-dimensional materials can be challenging, due to the large number of atoms required to form a moiré supercell without needing to apply unreasonably large strains to enforce commensurability for a periodic calculation. For our large-scale simulations of twisted bilayer $1T'$ WTe₂ we therefore employ linear scaling density functional theory (LS-DFT), as implemented in the ONETEP code [42]. For all ONETEP calculations we use a psinc-grid energy cutoff of 800 eV and cutoff radius of $13 a_0$ for the nonorthogonal generalized Wannier functions (NGWFs), settings known to be well-converged based studies on similar TMD systems with related composition [43,44]. Automated choices based on counting valence electrons in the PAW potentials result in 13 NGWFs on W atoms and 4 on Te atoms. No truncation is applied to the density kernel. Repeated images of the slab are placed 60 Å apart, with a cutoff applied to the Coulomb interaction in the out-of-plane direction to suppress any interaction between the repeated slabs [45,46]. We use the projector-augmented wave (PAW) method [47] with potentials from the JTH dataset [41]. We calculate unfolded spectral functions [48] for the twisted bilayers following a methodology, which adapts the approach to the NGWF representation, as described previously [49].

To form the crystal structure of the twisted bilayer, we take the relaxed monolayer geometry found using plane-wave DFT as described above, constructing a twisted bilayer using rigid copies of this monolayer, since at the twist angle we consider the moiré period is short enough that atomic reconstruction will be minimal [50]. We look for a supercell with a twist angle close to that measured in the aforementioned transport measurements [17,18]. We find a suitable supercell with a twist angle $\theta = 4.66^\circ$, close to the twist angles of the devices measured in Ref. [17]. The supercell contains 1848 atoms, and a maximum magnitude component of the strain tensor applied to one of the layers to ensure commensurability of 0.33%. For accurate energetics of the interlayer interactions, we employ the optB88-vdW [51] nonlocal van der Waals functional. The interlayer distance d is found by minimizing energy as a function of d between rigid monolayers. The result in this system is $d = 7.75 \text{ \AA}$, which is in line with expectations, being around 10% greater than the layer separation in bulk WTe₂ ($c = 7.035 \text{ \AA}$ [52]).

For interpretation of the stacking dependence of the band structure, we also perform plane-wave DFT band structures for aligned primitive bilayers of $1T'$ -WTe₂ for a selection of in-plane displacements. The same interlayer distance ($d = 7.75 \text{ \AA}$) from the twisted bilayer is carried over for these calculations, since at this relatively small moiré size, the interlayer distance is expected to remain roughly constant despite the changes in stacking through the unit cell.

III. RESULTS

A. Strain-dependent confining potential

To extract from our LS-DFT calculations for the twisted bilayer the changes in potential felt by electrons due to the moiré superlattice, we first perform calculations for each of the two isolated monolayers individually, with their atomic positions as in the twisted bilayer, then perform a calculation of the twisted bilayer. We then take the difference between the electrostatic potential in the twisted bilayer and the sum of the potentials of the isolated monolayers. The resulting quantity is specifically the change in potential due to the interaction and hybridization between states on the two layers. We show maps of the in-plane position dependence of this potential for z values corresponding to the mean planes of each layer in Fig. 3.

In TMDC bilayers marginally twisted from 3R stacking [53] it is known that equal-and-opposite potentials arise due to charge transfer between the layers, possible because of the layer asymmetry of the bilayer. Twisted bilayers of $1T'$ -WTe₂ behave rather differently: here the approximate local inversion symmetry of nearly parallel bilayer stacking requires the sign of the potential to be the same on the two layers. In Fig. 3 we see this confining potential for two cases: using constituent monolayers relaxed as described above, and a second case using monolayers biaxially strained by 1%. We choose biaxial strain to illustrate the sensitivity of the system to changes in the monolayer lattice parameter, since this choice leaves all other properties of the system, such as twist angle and supercell indices, unchanged. For the unstrained case we see only small changes (up to 20 meV) in the local electrostatic potential on formation of a twisted bilayer. On application of 1% strain the regime changes drastically, with the emergence of a striped potential landscape with a peak-to-trough strength ~ 200 meV. This striped pattern runs parallel to the stripes in the moiré pattern formed by varying displacement of the axes of the chains of tungsten atoms. The relative arrangements of the tellurium lattices, and local displacements along the tungsten chains, have minimal effect on the confining potential difference.

B. Unfolded spectral functions

Further insight can be obtained by plotting the spectral function for the twisted bilayer, unfolded and projected onto the primitive cells each of the two layers, as shown in Fig. 4. There is in the first instance a direct effect of heterostrain, namely that it shifts the unfolded bands on each layer relative to each other, as seen most clearly in the separation of blue and yellow bands: in the absence of any differential strain between the layers these would be superposed on each other. In our model, some heterostrain is already present in the nominally relaxed cell due to the strain that needs to be applied to one layer to form a commensurate unit cell. These differences are, however, small compared to other effects, and are only apparent in certain regions of the band structure, for example near the local maximum at the Γ point. Substantial changes to the bilayer band structure are apparent in comparison to the constituent monolayers. The minima of the electron pockets (states below the Fermi level arising from the conduction band

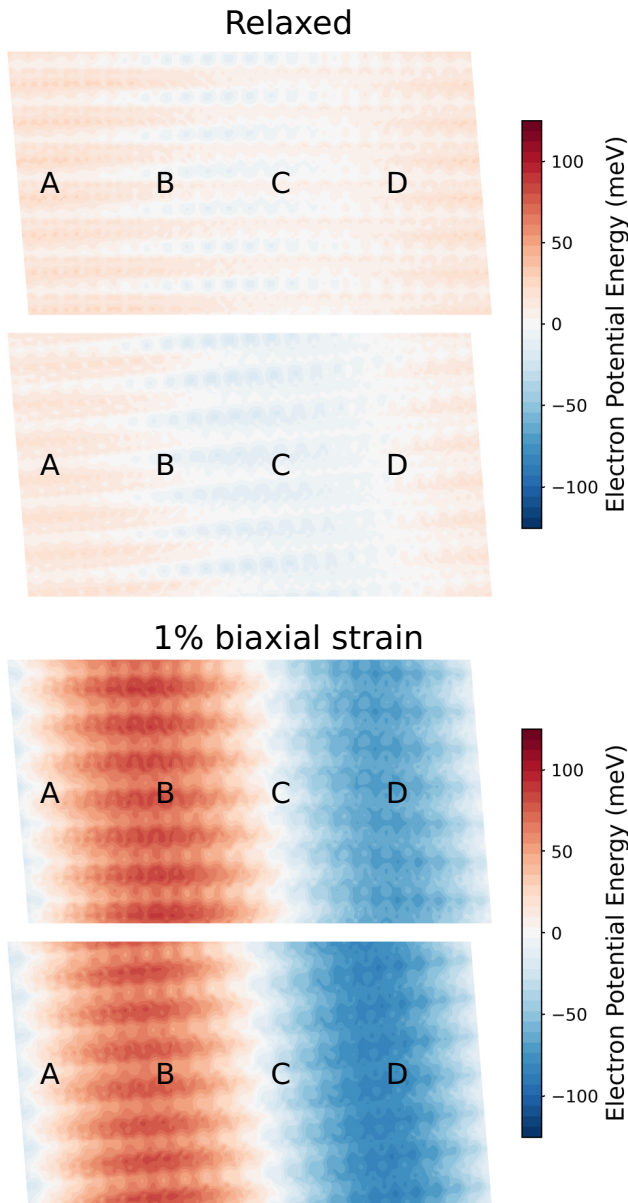


FIG. 3. Top two panels: Confining potentials in twisted bilayer $1T'$ - WTe_2 , calculated as the difference between electron potential energy of the twisted bilayer and the sum of the potentials from isolated monolayers with atomic positions taken from the bilayer. Top and bottom panels show potentials at mean planes of the two layers. Supercell is that shown in Fig. 2. Letters A–D indicate regions in which the local atomic registry approximates the aligned bilayer structures for which bands are calculated in Fig. 5. Bottom two panels: Same quantities, but for 1% strain applied to constituent monolayers.

minimum along the ΓX line) become detached from their bands, while below the valence band edge, the second band, which is particularly flat, is split into a standing wavelike structure. This can be interpreted as a breaking of the translational symmetry on the primitive cell scale as a function of position in the moiré cell, as induced by the 1D confining potential observed in Fig. 3. This effect is even stronger for the 1% biaxially strained case, where strong confining potential

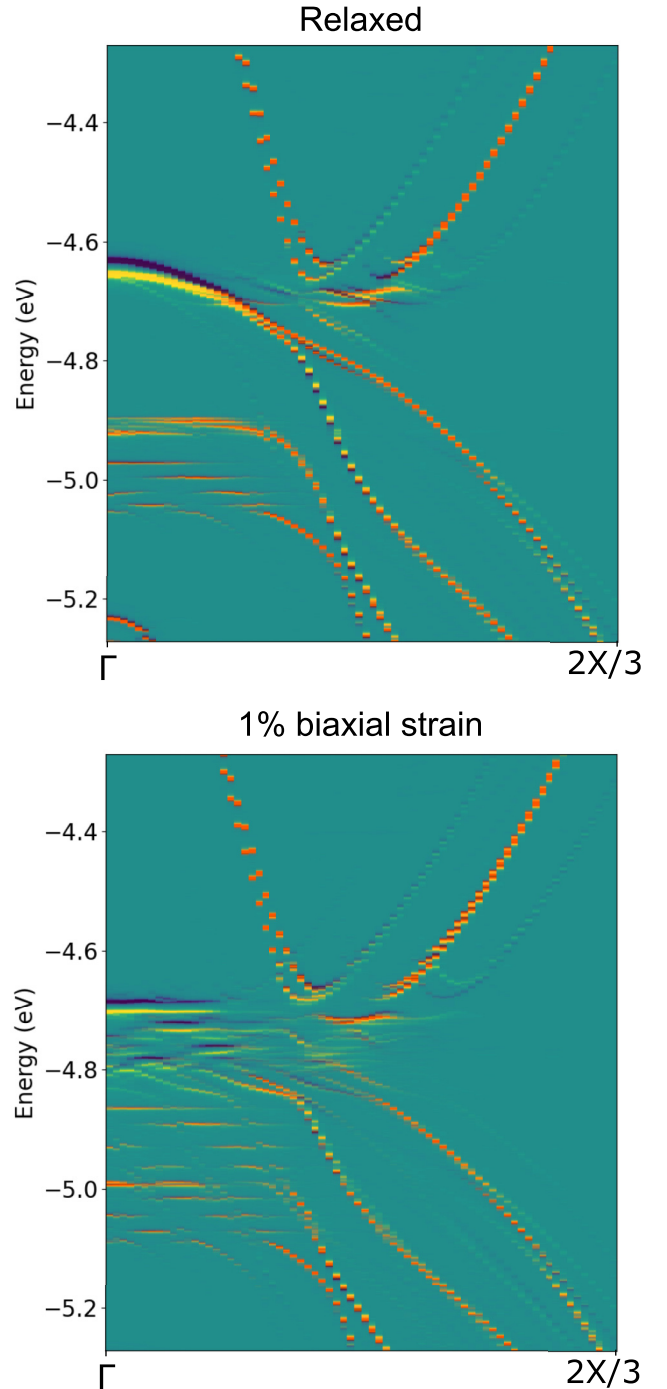


FIG. 4. Spectral function of twisted bilayer $1T'$ - WTe_2 , unfolded and projected onto primitive cells of each monolayer; yellow and blue bands correspond to projection on different layers, and add to orange where bands coincide. Spin-orbit coupling is taken into account perturbatively. Top and bottom panels are constructed from unstrained and 1% biaxially strained monolayers, respectively.

explored above causes the multiplicity of flat bands reaches to the top of the hole pockets (states above the Fermi level around Γ).

C. Strain induced Fermi-contour changes in aligned bilayers

Motivated by the appearance and strength of the confining potential on applying 1% biaxial strain, as well as by the

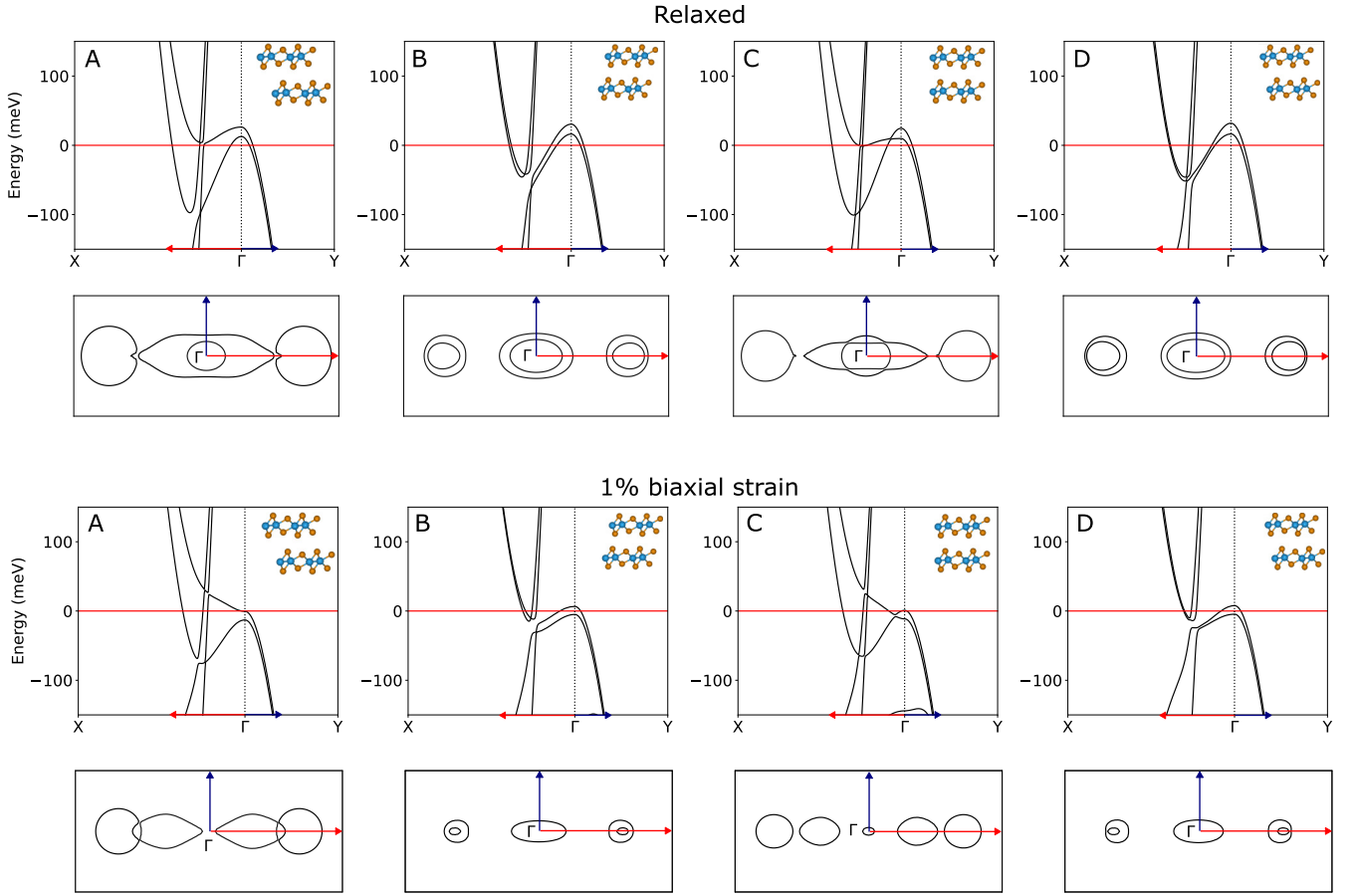


FIG. 5. Band structures and Fermi contours, neglecting spin-orbit coupling, for commensurate aligned bilayers of $1T'$ WTe_2 , with relative in-plane shifts of the layers taken from the local atomic registries found at the four points indicated in Figs. 2 and 3, and indicated schematically as insets. The interlayer distance is fixed as $d = 7.75 \text{ \AA}$. Top two rows are bands and Fermi contours calculated without strain, bottom rows are with 1% in-plane biaxial strain applied. Blue and red arrows indicate extent of regions mapped in the bottom panels to show Fermi contours.

pattern in the stacking dependence of interlayer hopping for aligned bilayers in Ref. [17], we calculate using plane-wave DFT bands and Fermi contours for aligned bilayers with stackings corresponding to the local stackings at the points marked A–D in Figs. 2 and 3 in the twisted bilayer. These we plot in Fig. 5.

While exactly at the top of the hole pocket at Γ the interlayer hopping changes very little for the different stacking configurations, towards X within the electron pockets the changes are substantial. In particular, the coupling changes sign on passing from configuration A to configuration C, necessarily passing through zero in the region of configurations B and D, where the layers become nearly electronically decoupled. This gives rise to topological transitions in the Fermi contour character depending on the local stacking in different regions of the moiré supercell in the twisted bilayer. The origin of these topological changes can therefore be interpreted to be the variation of coupling parameter as a function of stacking. Small changes in hybridization dramatically affects the relative position of the bands (particularly when including the effects of spin-orbit coupling) and thus the shape and extent of the electron and hole pockets vary strongly with stacking.

Owing to the reduction of overlap between electron and hole pockets, here, as in the monolayer [28], in the strained

case these changes become more critical. The Γ -point hole pocket dispersion becomes electronlike for the stacking (labeled A) for which the chain of tungsten atoms in one layer lies above the midpoint between two chains in the other. These transitions and the flat bands associated with them provide an indication of the origin of the instability to the formation of a moiré potential wave in the twisted bilayer.

In Fig. 5 the topological change of the Fermi contours on strain in the case of B and D stackings is that one of the two pockets at around Γ disappears upon straining the system. In the case though of A and D registries, the situation is more complicated with merging of parts of the Fermi contours, which may result in Van Hove singularities. The analysis of these singularities and their classification [54,55] is beyond the purpose of the present work and will be presented elsewhere. Note the possibility of Van Hove singularities in all cases of stacking, slightly away from the Fermi level.

IV. CONCLUSIONS

In conclusion, we have carried out a combination of linear-scaling and plane-wave DFT calculations for a twisted bilayer of $1T'$ - WTe_2 . By comparing the electrostatic potential map of an aligned bilayer with those of isolated monolayers we find that the one-dimensional stripes present in the moiré

pattern of the tungsten sublattices gives rise to an instability on application of a small strain to substantial confining potential wave with peak-to-trough magnitude ~ 200 meV, which comparison to quasi-1D organic semiconductors suggests is sufficient to drive LL behavior. The effects of this confining striped moiré pattern are readily apparent in the unfolded spectral functions of the twisted bilayer. Close examination of band structures from aligned bilayers with atomic registries corresponding to local stacking environments from different regions of the moiré superlattice shows notable changes to band structure and Fermi contour topologies depending on position in the moiré superlattice, particularly so for the slightly strained case. Our results focus on biaxial heterostrain, but there may be further physics to be uncovered via uniaxial strains. While we do not incorporate the in-plane nonuniform strain resulting from domain reconstructions that are known to be present in 2H TMDs [56], this is not expected to affect our conclusions because the nonuniform strains developed in simulations of such systems are very much smaller than those we use to illustrate the strain dependence of the band structure [57]. These computational results provide important theoretical underpinning for experimental results showing evidence of strong correlations in twisted 1T'-WTe₂ systems. It should be noted that the imprecision of DFT both in the determination of structural parameters and in band alignment and bandwidth for a given structure means that the results, which are closer to the behavior in a twisted bilayer studied in experiment may in fact be those which we have presented here as the strained case. Such twisted bilayers would therefore be unstable to the formation of a confining potential wave.

While we were able to neglect atomic reconstruction as we considered a comparatively large twist angle, for very small twist angles we would expect highly nonuniform strain in the moiré supercell as the structure distorts to minimize its total energy [56,58]. Given the sensitivity of 1T' WTe₂ to strain demonstrated here this would result in substantial changes to the electronic properties. Materials isostructural to WTe₂ in which similar phenomena might be expected include the quasi-one-dimensional tellurides Ta_{1.2}Os_{0.8}Te₄ [59], TaIrTe₄ [60,61], and NbIrTe₄ [62].

The research data supporting this publication can be accessed via the University of Warwicks research archive portal [63].

ACKNOWLEDGMENTS

The authors acknowledge useful discussions with A. Chandrasekaran and J. Betouras. The authors acknowledge funding from EPSRC Grant No. EP/V000136/1. Computing facilities were provided by the Scientific Computing Research Technology Platform of the University of Warwick through the use of the High Performance Computing (HPC) cluster Avon, and the Sulis Tier 2 platforms at HPC Midlands+ funded by the Engineering and Physical Sciences Research Council (EPSRC), Grant No. EP/T022108/1. Computational support was also obtained from the UK national high-performance computing service, ARCHER2, for which access was obtained via the UKCP consortium and funded by EPSRC Grant No. EP/X035891/1.

-
- [1] Y. Cao, V. Fatemi, S. Fang, K. Watanabe, T. Taniguchi, E. Kaxiras, and P. Jarillo-Herrero, Unconventional superconductivity in magic-angle graphene superlattices, *Nature (London)* **556**, 43 (2018).
 - [2] M. Yankowitz, S. Chen, H. Polshyn, Y. Zhang, K. Watanabe, T. Taniguchi, D. Graf, A. F. Young, and C. R. Dean, Tuning superconductivity in twisted bilayer graphene, *Science* **363**, 1059 (2019).
 - [3] A. L. Sharpe, E. J. Fox, A. W. Barnard, J. Finney, K. Watanabe, T. Taniguchi, M. A. Kastner, and D. Goldhaber-Gordon, Emergent ferromagnetism near three-quarters filling in twisted bilayer graphene, *Science* **365**, 605 (2019).
 - [4] M. Serlin, C. L. Tschirhart, H. Polshyn, Y. Zhang, J. Zhu, K. Watanabe, T. Taniguchi, L. Balents, and A. F. Young, Intrinsic quantized anomalous Hall effect in a moiré heterostructure, *Science* **367**, 900 (2020).
 - [5] M.-L. Lin, Q.-H. Tan, J.-B. Wu, X.-S. Chen, J.-H. Wang, Y.-H. Pan, X. Zhang, X. Cong, J. Zhang, W. Ji, P.-A. Hu, K.-H. Liu, and P.-H. Tan, Moiré phonons in twisted bilayer MoS₂, *ACS Nano* **12**, 8770 (2018).
 - [6] L. Wang, E.-M. Shih, A. Ghiotto, L. Xian, D. A. Rhodes, C. Tan, M. Claassen, D. M. Kennes, Y. Bai, B. Kim, K. Watanabe, T. Taniguchi, X. Zhu, J. Hone, A. Rubio, A. N. Pasupathy, and C. R. Dean, Correlated electronic phases in twisted bilayer transition metal dichalcogenides, *Nat. Mater.* **19**, 861 (2020).
 - [7] Y. Tang, L. Li, T. Li, Y. Xu, S. Liu, K. Barmak, K. Watanabe, T. Taniguchi, A. H. MacDonald, J. Shan, and K. F. Mak, Simulation of Hubbard model physics in WSe₂/WS₂ moiré superlattices, *Nature (London)* **579**, 353 (2020).
 - [8] E. C. Regan, D. Wang, C. Jin, M. I. B. Utama, B. Gao, X. Wei, S. Zhao, W. Zhao, Z. Zhang, K. Yumigeta, M. Blei, J. D. Carlström, K. Watanabe, T. Taniguchi, S. Tongay, M. Crommie, A. Zettl, and F. Wang, Mott and generalized Wigner crystal states in WSe₂/WS₂ moiré superlattices, *Nature (London)* **579**, 359 (2020).
 - [9] J. Quan, L. Linhart, M.-L. Lin, D. Lee, J. Zhu, C.-Y. Wang, W.-T. Hsu, J. Choi, J. Embley, C. Young, T. Taniguchi, K. Watanabe, C.-K. Shih, K. Lai, A. H. MacDonald, P.-H. Tan, F. Libisch, and X. Li, Phonon renormalization in reconstructed MoS₂ moiré superlattices, *Nat. Mater.* **20**, 1100 (2021).
 - [10] F. Ferreira, S. J. Magorrian, V. V. Enaldiev, D. A. Ruiz-Tijerina, and V. I. Fal'ko, Band energy landscapes in twisted homobilayers of transition metal dichalcogenides, *Appl. Phys. Lett.* **118**, 241602 (2021).
 - [11] A. Sinner, P. A. Pantaleón, and F. Guinea, Strain-induced quasi-1D channels in twisted moiré lattices, *Phys. Rev. Lett.* **131**, 166402 (2023).
 - [12] F. Escudero, A. Sinner, Z. Zhan, P. A. Pantaleón, and F. Guinea, Designing moiré patterns by strain, *Phys. Rev. Res.* **6**, 023203 (2024).
 - [13] D. M. Kennes, L. Xian, M. Claassen, and A. Rubio, One-dimensional flat bands in twisted bilayer germanium selenide, *Nat. Commun.* **11**, 1124 (2020).

- [14] I. Soltero, J. Guerrero-Sánchez, F. Mireles, and D. A. Ruiz-Tijerina, Moiré band structures of twisted phosphorene bilayers, *Phys. Rev. B* **105**, 235421 (2022).
- [15] K.-A. N. Duerloo, Y. Li, and E. J. Reed, Structural phase transitions in two-dimensional Mo- and W-dichalcogenide monolayers, *Nat. Commun.* **5**, 4214 (2014).
- [16] E. Torun, H. Sahin, S. Cahangirov, A. Rubio, and F. M. Peeters, Anisotropic electronic, mechanical, and optical properties of monolayer WTe₂, *J. Appl. Phys.* **119**, 074307 (2016).
- [17] P. Wang, G. Yu, Y. H. Kwan, Y. Jia, S. Lei, S. Klemenz, F. A. Cevallos, R. Singha, T. Devakul, K. Watanabe, T. Taniguchi, S. L. Sondhi, R. J. Cava, L. M. Schoop, S. A. Parameswaran, and S. Wu, One-dimensional Luttinger liquids in a two-dimensional moiré lattice, *Nature (London)* **605**, 57 (2022).
- [18] G. Yu, P. Wang, A. J. Uzan-Narovlansky, Y. Jia, M. Onyszczyk, R. Singha, X. Gui, T. Song, Y. Tang, K. Watanabe *et al.*, Evidence for two dimensional anisotropic Luttinger liquids at millikelvin temperatures, *Nat. Commun.* **14**, 7025 (2023).
- [19] I. V. Lerner, B. L. Althsuler, V. I. Fal'ko, and T. Giamarchi, *Strongly Correlated Fermions and Bosons in Low-Dimensional Disordered Systems* (Springer Science & Business Media, Berlin, 2002), Vol. 72.
- [20] X. Qian, J. Liu, L. Fu, and J. Li, Quantum spin Hall effect in two-dimensional transition metal dichalcogenides, *Science* **346**, 1344 (2014).
- [21] F. Zheng, C. Cai, S. Ge, X. Zhang, X. Liu, H. Lu, Y. Zhang, J. Qiu, T. Taniguchi, K. Watanabe, S. Jia, J. Qi, J.-H. Chen, D. Sun, and J. Feng, On the quantum spin Hall gap of monolayer 1T'-WTe₂, *Adv. Mater.* **28**, 4845 (2016).
- [22] Z. Fei, T. Palomaki, S. Wu, W. Zhao, X. Cai, B. Sun, P. Nguyen, J. Finney, X. Xu, and D. H. Cobden, Edge conduction in monolayer WTe₂, *Nat. Phys.* **13**, 677 (2017).
- [23] S. Tang, C. Zhang, D. Wong, Z. Pedramrazi, H.-Z. Tsai, C. Jia, B. Moritz, M. Claassen, H. Ryu, S. Kahn, J. Jiang, H. Yan, M. Hashimoto, D. Lu, R. G. Moore, C.-C. Hwang, C. Hwang, Z. Hussain, Y. Chen, M. M. Ugeda *et al.*, Quantum spin Hall state in monolayer 1T'-WTe₂, *Nat. Phys.* **13**, 683 (2017).
- [24] Z.-Y. Jia, Y.-H. Song, X.-B. Li, K. Ran, P. Lu, H.-J. Zheng, X.-Y. Zhu, Z.-Q. Shi, J. Sun, J. Wen, D. Xing, and S.-C. Li, Direct visualization of a two-dimensional topological insulator in the single-layer 1T' - WTe₂, *Phys. Rev. B* **96**, 041108(R) (2017).
- [25] I. Cucchi, I. Gutiérrez-Lezama, E. Cappelli, S. M. Walker, F. Y. Bruno, G. Ténasini, L. Wang, N. Ubrig, C. Barreateau, E. Giannini, M. Gibertini, A. Tamai, A. F. Morpurgo, and F. Baumberger, Microfocus laser-angle-resolved photoemission on encapsulated mono-, bi-, and few-layer 1T' WTe₂, *Nano Lett.* **19**, 554 (2019).
- [26] S. Wu, V. Fatemi, Q. D. Gibson, K. Watanabe, T. Taniguchi, R. J. Cava, and P. Jarillo-Herrero, Observation of the quantum spin Hall effect up to 100 kelvin in a monolayer crystal, *Science* **359**, 76 (2018).
- [27] Y. Shi, J. Kahn, B. Niu, Z. Fei, B. Sun, X. Cai, B. A. Francisco, D. Wu, Z.-X. Shen, X. Xu, D. H. Cobden, and Y.-T. Cui, Imaging quantum spin Hall edges in monolayer WTe₂, *Sci. Adv.* **5**, eaat8799 (2019).
- [28] C. Zhao, M. Hu, J. Qin, B. Xia, C. Liu, S. Wang, D. D. Guan, Y. Li, H. Zheng, J. Liu, and J. Jia, Strain tunable semimetal-topological-insulator transition in monolayer 1T'-WTe₂, *Phys. Rev. Lett.* **125**, 046801 (2020).
- [29] Y. Jia, P. Wang, C.-L. Chiu, Z. Song, G. Yu, B. Jäck, S. Lei, S. Klemenz, F. A. Cevallos, M. Onyszczyk, N. Fishchenko, X. Liu, G. Farahi, F. Xie, Y. Xu, K. Watanabe, T. Taniguchi, B. A. Bernevig, R. J. Cava *et al.*, Evidence for a monolayer excitonic insulator, *Nat. Phys.* **18**, 87 (2022).
- [30] B. Sun, W. Zhao, T. Palomaki, Z. Fei, E. Runburg, P. Malinowski, X. Huang, J. Cenker, Y.-T. Cui, J.-H. Chu, X. Xu, S. S. Ataei, D. Varsano, M. Palummo, E. Molinari, M. Rontani, and D. H. Cobden, Evidence for equilibrium exciton condensation in monolayer WTe₂, *Nat. Phys.* **18**, 94 (2022).
- [31] Z. Fei, W. Zhao, T. A. Palomaki, B. Sun, M. K. Miller, Z. Zhao, J. Yan, X. Xu, and D. H. Cobden, Ferroelectric switching of a two-dimensional metal, *Nature (London)* **560**, 336 (2018).
- [32] P. Sharma, F.-X. Xiang, D.-F. Shao, D. Zhang, E. Y. Tsymlal, A. R. Hamilton, and J. Seidel, A room-temperature ferroelectric semimetal, *Sci. Adv.* **5**, eaax5080 (2019).
- [33] Q. Yang, M. Wu, and J. Li, Origin of two-dimensional vertical ferroelectricity in WTe₂ bilayer and multilayer, *J. Phys. Chem. Lett.* **9**, 7160 (2018).
- [34] X. Liu, Y. Yang, T. Hu, G. Zhao, C. Chen, and W. Ren, Vertical ferroelectric switching by in-plane sliding of two-dimensional bilayer WTe₂, *Nanoscale* **11**, 18575 (2019).
- [35] C.-L. Lin, R. Arafune, R.-Y. Liu, M. Yoshimura, B. Feng, K. Kawahara, Z. Ni, E. Minamitani, S. Watanabe, Y. Shi *et al.*, Visualizing type-II Weyl points in tungsten ditelluride by quasiparticle interference, *ACS Nano* **11**, 11459 (2017).
- [36] Y. Zhang, K. Kamiya, T. Yamamoto, M. Sakano, X. Yang, S. Masubuchi, S. Okazaki, K. Shinokita, T. Chen, K. Aso, Y. Yamada-Takamura, Y. Oshima, K. Watanabe, T. Taniguchi, K. Matsuda, T. Sasagawa, K. Ishizaka, and T. Machida, Symmetry engineering in twisted bilayer WTe₂, *Nano Lett.* **23**, 9280 (2023).
- [37] P. Giannozzi, S. Baroni, N. Bonini, M. Calandra, R. Car, C. Cavazzoni, D. Ceresoli, G. L. Chiarotti, M. Cococcioni, I. Dabo, A. D. Corso, S. de Gironcoli, S. Fabris, G. Fratesi, R. Gebauer, U. Gerstmann, C. Gougoussis, A. Kokalj, M. Lazzeri, L. Martin-Samos *et al.*, QUANTUM ESPRESSO: a modular and open-source software project for quantum simulations of materials, *J. Phys.: Condens. Matter* **21**, 395502 (2009).
- [38] P. Giannozzi Jr, O. Andreussi, T. Brumme, O. Bunau, M. B. Nardelli, M. Calandra, R. Car, C. Cavazzoni, D. Ceresoli, M. Cococcioni, N. Colonna, I. Carnimeo, A. D. Corso, S. de Gironcoli, P. Delugas, R. A. DiStasio, A. Ferretti, A. Floris, G. Fratesi, G. Fugallo *et al.*, Advanced capabilities for materials modelling with QUANTUM ESPRESSO, *J. Phys.: Condens. Matter* **29**, 465901 (2017).
- [39] J. P. Perdew, K. Burke, and M. Ernzerhof, Generalized gradient approximation made simple, *Phys. Rev. Lett.* **77**, 3865 (1996).
- [40] A. Dal Corso, Pseudopotentials periodic table: From H to Pu, *Comput. Mater. Sci.* **95**, 337 (2014).
- [41] F. Jollet, M. Torrent, and N. Holzwarth, Generation of projector augmented-wave atomic data: A 71 element validated table in the XML format, *Comput. Phys. Commun.* **185**, 1246 (2014).
- [42] J. C. A. Prentice, J. Aarons, J. C. Womack, A. E. A. Allen, L. Andrinopoulos, L. Anton, R. A. Bell, A. Bhandari, G. A. Bramley, R. J. Charlton, R. J. Clements, D. J. Cole, G. Constantinescu, F. Corsetti, S. M.-M. Dubois, K. K. B. Duff, J. M. Escartín, A. Greco, Q. Hill, L. P. Lee *et al.*, The ONETEP linear-scaling density functional theory program, *J. Chem. Phys.* **152**, 174111 (2020).

- [43] S. M. Loh, X. Xia, N. R. Wilson, and N. D. M. Hine, Strong in-plane anisotropy in the electronic properties of doped transition metal dichalcogenides exhibited in $W_{1-x}Nb_xS_2$, *Phys. Rev. B* **103**, 245410 (2021).
- [44] X. Xia, S. M. Loh, J. Viner, N. C. Teutsch, A. J. Graham, V. Kandyba, A. Barinov, A. M. Sanchez, D. C. Smith, N. D. M. Hine, and N. R. Wilson, Atomic and electronic structure of two-dimensional $Mo_{(1-x)}W_xS_2$ alloys, *J. Phys. Mater.* **4**, 025004 (2021).
- [45] C. A. Rozzi, D. Varsano, A. Marini, E. K. U. Gross, and A. Rubio, Exact Coulomb cutoff technique for supercell calculations, *Phys. Rev. B* **73**, 205119 (2006).
- [46] N. D. M. Hine, J. Dziedzic, P. D. Haynes, and C.-K. Skylaris, Electrostatic interactions in finite systems treated with periodic boundary conditions: Application to linear-scaling density functional theory, *J. Chem. Phys.* **135**, 204103 (2011).
- [47] N. D. M. Hine, Linear-scaling density functional theory using the projector augmented wave method, *J. Phys.: Condens. Matter* **29**, 024001 (2017).
- [48] V. Popescu and A. Zunger, Extracting E versus \vec{k} effective band structure from supercell calculations on alloys and impurities, *Phys. Rev. B* **85**, 085201 (2012).
- [49] G. C. Constantinescu and N. D. M. Hine, Energy landscape and band-structure tuning in realistic $MoS_2/MoSe_2$ heterostructures, *Phys. Rev. B* **91**, 195416 (2015).
- [50] F. Yuan, Y. Jia, G. Cheng, R. Singha, S. Lei, N. Yao, S. Wu, and L. M. Schoop, Atomic resolution imaging of highly air-sensitive monolayer and twisted-bilayer WTe_2 , *Nano Lett.* **23**, 6868 (2023).
- [51] J. Klimeš, D. R. Bowler, and A. Michaelides, Chemical accuracy for the van der Waals density functional, *J. Phys.: Condens. Matter* **22**, 022201 (2010).
- [52] B. E. Brown, The crystal structures of WTe_2 and high-temperature $MoTe_2$, *Acta Crystallogr.* **20**, 268 (1966).
- [53] F. Ferreira, V. V. Enaldiev, V. I. Fal'ko, and S. J. Magorrian, Weak ferroelectric charge transfer in layer-asymmetric bilayers of 2D semiconductors, *Sci. Rep.* **11**, 13422 (2021).
- [54] A. Chandrasekaran, A. Shtyk, J. J. Betouras, and C. Chamon, Catastrophe theory classification of Fermi surface topological transitions in two dimensions, *Phys. Rev. Res.* **2**, 013355 (2020).
- [55] A. Chandrasekaran and J. J. Betouras, A practical method to detect, analyze, and engineer higher order Van Hove singularities in multi-band Hamiltonians, *Adv. Phys. Res.* **2**, 2200061 (2023).
- [56] A. Weston, Y. Zou, V. Enaldiev, A. Summerfield, N. Clark, V. Zólyomi, A. Graham, C. Yelgel, S. Magorrian, M. Zhou, J. Zultak, D. Hopkinson, A. Barinov, T. H. Bointon, A. Kretinin, N. R. Wilson, P. H. Beton, V. I. Fal'ko, S. J. Haigh, and R. Gorbachev, Atomic reconstruction in twisted bilayers of transition metal dichalcogenides, *Nat. Nanotechnol.* **15**, 592 (2020).
- [57] F. M. Arnold, A. Ghasemifard, A. Kuc, J. Kunstmann, and T. Heine, Relaxation effects in twisted bilayer molybdenum disulfide: structure, stability, and electronic properties, *2D Mater.* **10**, 045010 (2023).
- [58] J. Hagel, S. Brem, J. A. Pineiro, and E. Malic, Impact of atomic reconstruction on optical spectra of twisted TMD homobilayers, *Phys. Rev. Mater.* **8**, 034001 (2024).
- [59] W.-H. Jiao, S. Xiao, S.-J. Zhang, W.-Z. Yang, X.-M. Xie, Y. Liu, J.-Y. Liu, S.-J. Song, W. Liu, Z. Ren, G.-H. Cao, X. Xu, and S. He, Structure and transport properties of the quasi-one-dimensional telluride $Ta_{1.2}Os_{0.8}Te_4$, *Phys. Rev. B* **105**, 064201 (2022).
- [60] Y. Xing, Z. Shao, J. Ge, J. Luo, J. Wang, Z. Zhu, J. Liu, Y. Wang, Z. Zhao, J. Yan, D. Mandrus, B. Yan, X.-J. Liu, M. Pan, and J. Wang, Surface superconductivity in the type II Weyl semimetal $TaIrTe_4$, *Natl. Sci. Rev.* **7**, 579 (2020).
- [61] P.-J. Guo, X.-Q. Lu, W. Ji, K. Liu, and Z.-Y. Lu, Quantum spin Hall effect in monolayer and bilayer $TaIrTe_4$, *Phys. Rev. B* **102**, 041109(R) (2020).
- [62] X. Liu, J. Lai, J. Zhan, T. Yu, W. Shi, P. Liu, X.-Q. Chen, and Y. Sun, Prediction of dual quantum spin Hall insulator in $NbIrTe_4$ monolayer, [arXiv:2406.00979](https://arxiv.org/abs/2406.00979).
- [63] Warwick Research Archive Portal, <https://wrap.warwick.ac.uk/186456/>.